Melting transition of Lennard-Jones fluid in cylindrical pores

Chandan K. Das, and Jayant K. Singh

View Online   Export Citation   CrossMark

ARTICLES YOU MAY BE INTERESTED IN

Melting transition of Lennard-Jones fluid in cylindrical pores

Chandan K. Das and Jayant K. Singh[a)]
Department of Chemical Engineering, Indian Institute of Technology Kanpur, Kanpur 208016, India

Three-stage pseudo-supercritical transformation path and multiple-histogram reweighting technique are employed for the determination of solid-liquid coexistence of the Lennard-Jones (12-6) fluid, in a structureless cylindrical pore of radius, R, ranging from 4 to 20 molecular diameters. The Gibbs free energy difference is evaluated using thermodynamic integration method by connecting solid and liquid phases under confinement via one or more intermediate states without any first order phase transition among them. The thermodynamic melting temperature, T_m, is found to oscillate for pore size, R < 8, which is in agreement with the behavior observed for the melting temperature in slit pores. However, T_m for almost all pore sizes is less than the bulk case, which is contrary to the behavior seen for the slit pore. The oscillation in T_m decays at around pore radius $R = 8$, and beyond that shift in the melting temperature with respect to the bulk case is in line with the prediction of the Gibbs-Thomson equation. © 2014 AIP Publishing LLC. [http://dx.doi.org/10.1063/1.4876077]

I. INTRODUCTION

The melting/freezing phenomena of confined fluids play an important role in nature as in frost heaving, weathering of rocks,[1] and biology.[2] Further, it is relevant to various fields of modern technology such as micro-fluidics, fabrication of nanomaterials, adhesion, nanotribology, and nanotechnology.[3] Hence, various studies have been conducted in order to understand the solid-liquid transition under confinement.[4]

It is well known that, in presence of surfaces, the competition between fluid–wall and fluid–fluid interactions can lead to interesting phenomena.[5–7] Examples include, capillary condensation,[8–10] shift in vapor-liquid critical temperature,[11–15] anomalous variation in vapor-liquid critical density, prewetting,[16] layering, and wetting transition.[17] On the other hand, the freezing temperature can get suppressed or enhanced under confinement,[7,18–22] as seen in numerous experiments.[6,23–33] For example, depression in the freezing temperature is observed for oxygen in sol–gel glasses of pore size distribution 2.2–18.7 nm.[28] Similarly, the freezing and melting temperatures of indium are less compared to the bulk value, and vary inversely with pore diameter in porous silica glasses.[24] In contrast to these results for glasses, a significant increase in the melting temperature is reported for cyclohexane and octamethylcyclotetrasiloxane in mica pore.[25] The pore size dependent shift in the melting temperature of water in cylindrical silica nanopores, estimated using differential scanning calorimetry, is well represented by the Gibbs-Thomson equation, and the hysteresis associated with the phase transition is found to disappear near a pore diameter $\approx$2.8 nm.[34]

Numerous molecular simulation techniques have been implemented to understand the freezing and melting behavior of confined molecular systems.[4,5,35,36] In case of bulk

solid, heuristic methods such as Lindemann parameter,[37,38] Born criteria (bulk),[39] non-Gaussian parameter[37] have been used successfully. In other cases, structural parameters, such as static order parameter,[40] structure factor,[7,41–44] radial distribution function, and orientational correlation function[20,45] are most commonly used parameters for determination of the melting/freezing temperature. On the other hand, solid-liquid coexistence temperature in confinement can be evaluated effectively and accurately from free energy difference using thermodynamic integration[20,46,47] for simple systems.

The freezing/melting behavior of confined fluids has been related to the variation in the ratio of wall–fluid and fluid–fluid interactions based on the Landau theory and order parameter formulation.[46,48] Earlier studies[5,7,22,25,28,47] on confined solid in slit pore showed that the elevation and depression of the melting/freezing temperatures are inversely proportional to the slit separation. On the other hand, recent works of Kaneko *et al.*[22] and Wan *et al.*[49] report an oscillatory behavior of the melting and freezing temperatures with the pore size. Oscillatory nature of the melting temperature is also observed in our earlier work.[18] These results question an earlier believed linear nature of the melting/freezing temperature with inverse of the pore size, and its extensibility to extremely narrow pores. In our previous work, we have reported the thermodynamic melting transition of Lennard-Jones solid in confined slit pores, based on a free-energy approach.[19] We also observed that at higher pore sizes, the melting phenomenon follows the Gibbs-Thomson equation. However, it is not clear if the observation seen for the slit pore also holds for higher degree of confinement, i.e., cylindrical and spherical confinement.

The effects of the cylindrical confinement on the freezing/melting of simple fluids have been studied using experiments and molecular simulation.[20,45,50] Molecular dynamics simulations have been used to understand the solid-liquid transition of hard sphere[51] and square-well fluids.[52] In addition, earlier works have focused on understanding the

---

a)Author to whom correspondence should be addressed. Electronic mail: jayantks@iitk.ac.in

structural properties,[51,53] capillary condensation,[9,10] and density profile[16,54] for simple systems. However, insight into the behavior of solid-liquid coexistence temperature in cylindrical pores[20,45,50] have been less traced, and still not well characterized. In addition, the relationship between pore size and melting temperature is still not clear, and validity of the Gibbs-Thomson equation for extremely narrow pore is yet to be verified. To address the above, in this work, we extend the methodology developed recently based on pseudo-critical transformation path along with multiple histogram reweighting (MHR)[19] to locate the thermodynamic melting temperature of a LJ solid in cylindrical pores, ranging from 4 to 20 molecular diameters in radius. The rest of the paper is organized as follows. The model and method are described in Sec. II. In Sec. III, some details of the simulations are provided, and in Sec. IV, the results are presented and discussed. Finally, concluding remarks are presented in Sec. V.

II. MODEL AND METHODS

A. Potential models

The fluid–fluid interaction is modeled by the truncated and shifted LJ potential:

$$U_{ff}^{tr-sh} = \begin{cases} U_{ff}^{lj}(r) - U_{ff}^{lj}(r_c) & r \leq r_c \\ 0 & r > r_c \end{cases}, \quad (1)$$

where

$$U_{ff}^{lj}(r) = 4\varepsilon_{ff}\left[\left(\frac{\sigma_{ff}}{r}\right)^{12} - \left(\frac{\sigma_{ff}}{r}\right)^{6}\right],$$

where σ_{ff} is the particle diameter, ε_{ff} is the interaction well depth, and r is the distance between two particles. Cut-off radius, r_c, is fixed at $5\sigma_{ff}$.

In this work, the pore is modeled as a structureless cylindrical pore. The cylindrical boundary is generated by putting a concentric cylinder inside an orthogonal simulation box, where the particles are initially packed, but cropped out based on the boundary of curved surface of the cylinder. This is followed by an equilibration run at a given temperature and pressure (see Figure 1). The type of interaction potential is a cylindrical analog of a graphitic slit pore,[55,56] where interaction between the wall and a fluid particle at a distance r is defined by LJ 9-3 potential.[6] The potential form is as follows:[55]

$$U_{wf}(r) = \frac{2}{3}\pi\rho_w\varepsilon_{wf}\sigma_{wf}^3\left[\frac{2}{15}\left(\frac{\sigma_{wf}}{r}\right)^9 - \left(\frac{\sigma_{wf}}{r}\right)^3\right], \quad (2)$$

where ρ_w is the number density of atoms in the wall, the subscripts f and w represent fluid and wall, respectively. σ_{wf} and ε_{wf} are the cross parameters for the wall-fluid interaction. In this work, we fix $\sigma_{ff} = 1$, $\varepsilon_{ff} = 1$, $\sigma_{ww} = 0.8924$, $\varepsilon_{ww} = 0.1891$, $\rho_w = 6.3049$, $\sigma_{wf} = (\sigma_{ff} + \sigma_w)/2$, and $\varepsilon_{wf} = (\varepsilon_{ff}\varepsilon_{ww})^{0.5}$, as per Refs. 7 and 19. The strength of interaction of the wall-fluid relative to the fluid-fluid interaction is define by the coefficient, $\alpha = \rho_w\varepsilon_{wf}\sigma_{wf}^3/\varepsilon_{ff}$, which is fixed at 2.32. LJ 9-3 pore radius is varied from 4 to 20 molecular diameters. In this work, all quantities are reduced with respect to σ_{ff} and ε_{ff}.
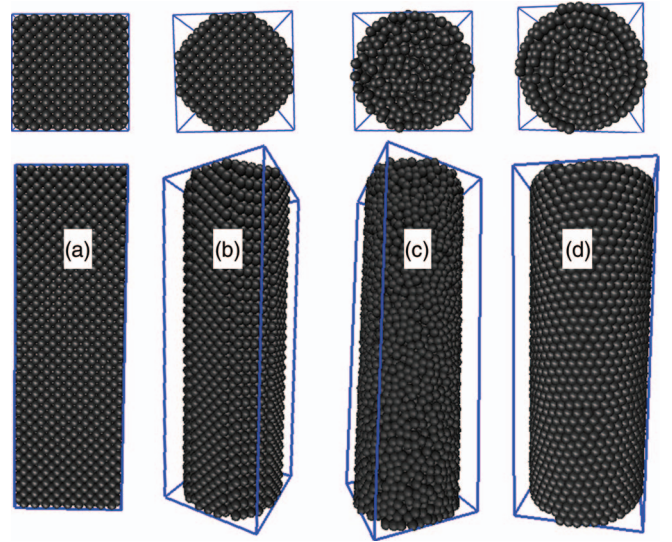

FIG. 1. Snapshots of constructing simulations of particles confined in cylindrical pores: (a) initial generation of FCC packing at high density in orthogonal shape in accordance with required size, (b) remove particles outside of the cylindrical pore, (c) randomly remove additional particles to satisfy the density, and (d) perfect cylindrical pore shape after few equilibrium simulation run. The top row represents the cross-sectional view and the bottom row presents the side view.

B. Simulation methodologies

In this work, we extend the method employed for slit pores to cylindrical pores. The detailed methodology is given in Refs. 19 and 57. However, we present briefly the method for the sake of completion, and to provide modifications necessary to adapt the method for cylindrical pores.

The estimation of melting temperature from free energy analysis comprising four steps: (a) estimation of an approximate melting temperature from a thermal cycle; (b) computation of equation of state for the solid and liquid phases using multiple-histogram reweighting method at a reference state point; (c) the determination of difference in free energy between solid and liquid phases at an approximate melting temperature using the pseudo-supercritical transformation path; (d) and finally, using steps (b) and (c), evaluating the melting temperature where Gibbs free energy is zero. Each step is described below in detail.

1. Estimation of an approximate melting point

To locate an approximate melting point, we progressively heat and quench solid and liquid phases, respectively, using an isothermal-isobaric ensemble ($NP_{zz}AT$) at $P_{zz} = 1.0$. Subsequently, the approximate melting point is selected within the hysteresis loop at which an abrupt change in the density is observed.

2. Solid and liquid equation of state

The second step is the generation of the Gibbs free energy as a function of temperature for the solid and liquid phases with respect to their respective reference state point over a small temperature range around the approximate

melting temperature at a constant pressure. With the help of free energy difference between the two phases, at the approximate melting temperature, the pure phase relative free energy curves can be converted to the solid-liquid free energy difference as a function of temperature. This further can be used to estimate the temperature where the free energy is equal for both the solid and liquid phases. This is done using the MHR technique.[19,57–63]

3. Determination of solid-liquid free energy difference at the approximate melting temperature

The Helmholtz free energy difference between the solid and liquid phases at an approximate melting temperature is computed by constructing a reversible thermodynamic path between the solid and liquid phases through one or more intermediate states.[64] The free energy along this pseudo-supercritical path is computed with a standard thermodynamic integration procedure:

$$\Delta A^{ex} = \int \left\langle \frac{dU}{d\lambda} \right\rangle_{NVT\lambda} d\lambda, \tag{3}$$

where ΔA^{ex} is the difference in excess Helmholtz free energy and λ is the Kirkwood's coupling parameter. Typically λ vary from zero to 1 such that when $\lambda = 0$ system act as a reference state, and angled bracket indicates the *NVT* ensemble average for a particular value of λ. The schematic representation of three-stage pseudo-supercritical transformation path is presented in Fig. 2. Brief description of the steps is given below.

a. Stage-a In the first step, fully interacting liquid is transferred to a weakly interacting fluid by means of a coupling parameter λ, which scales intermolecular interactions in the following manner:

$$U_a(\lambda) = [1 - \lambda(1 - \eta)]U_{\text{inter}}(r^N) + \phi_{fw}, \tag{4}$$

where $U_{inter}(\mathbf{r}^N)$ is the intermolecular potential energy based on the positions of all N particles, ϕ_{fw} represents potential
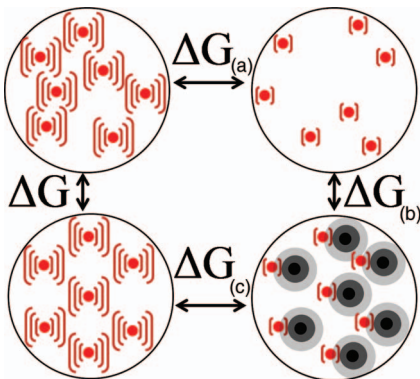

FIG. 2. The schematic representation of the three-stage pseudo-supercritical transformation path for the cylindrical confined system. (a) The liquid phase is converted to a weakly interacting fluid by gradually reducing the intermolecular interactions. (b) Gaussian potential wells are turned on while the volume is reduced to achieve a weakly interacting ordered phase. (c) Gaussian wells are turned off while simultaneously intermolecular interactions are gradually restored to achieve a crystalline phase.

energy due to wall-fluid interaction, independent of coupling parameter, and η is a scaling parameter such that $0 < \eta < 1$. The derivative of this function yields

$$\frac{\partial U_a}{\partial \lambda} = -(1 - \eta)U_{\text{inter}}(r^N). \tag{5}$$

b. Stage-b In the second stage, the simulation box volume is reduced from the liquid phase volume to the solid phase volume. Hence, axial length of the cylinder (L_z) for a given pore size must be known at the apparent melting temperature, either from the MHR results or from isothermal-isobaric simulation runs. This ensures that the pressure in the z direction of liquid and solid phases is equal at the beginning of stage-a and at the end of the transformation path. The potential energy based on λ for this stage is

$$U_b(\lambda) = \eta U_{\text{inter}}[r^N(\lambda)] + \lambda U_{Gauss}[r^N(\lambda), r^N_{well}(\lambda)] + \phi_{fw}, \tag{6}$$

where $\mathbf{r}^N(\lambda)$ and $\mathbf{r}_{well}{}^N(\lambda)$ are the Cartesian coordinates of the particles and potential wells, respectively, which is a function of λ due to the variable box volume. U_{Gauss} represents potential energy due to the interaction between the Gaussian potential wells and particles; and ϕ_{fw} represents the potential energy due to the wall-fluid interaction. To relate change in the Cartesian coordinates to the change in box volume, we follow the similar procedure as described in our earlier work.[19]

c. Stage-c This is the final stage of the pseudo-supercritical transformation path. We now have a fluid constrained to the configurational space of its solid phase. The potential energy function of this final stage as a function of λ is

$$U_c(\lambda) = [\eta + (1 - \eta)\lambda]U_{\text{inter}}(r^N)$$
$$+ (1 - \lambda)U_{Gauss}(r^N, r^N_{well}) + \phi_{fw}, \tag{7}$$

and the derivative is given by

$$\frac{\partial U_c}{\partial \lambda} = (1 - \eta)U_{\text{inter}}(r^N) - U_{Gauss}(r^N, r^N_{well}). \tag{8}$$

4. Finding the temperature where ΔG is zero

The difference in the excess Helmholtz free energy ΔA^{ex}, between the crystalline and liquid phases, at the approximate melting temperature, is determined in the previous steps a–c by thermodynamic integration using three-stage pseudo-supercritical path. It is required to convert the Helmholtz free energy to the Gibbs free energy, which is done through a simple relationship, $\Delta G = \Delta A^{ex} + \Delta A^{id} + P_{zz}A\Delta(L_z)$, where the term ΔA^{ex} is yielded from the three-stage pseudo-supercritical transformation path method, ΔA^{id} is the change in the ideal gas contribution to the Helmholtz free energy, P_{zz} is the pressure in axial direction of the pore, and A is the cross sectional area of the pore. Additionally, the histogram reweighting analysis yields two free energy curves. For the liquid phase, $\{(\beta G)_{T_1,l} - (\beta G)_{T_i,l}\}$ is known and for the solid phase, $\{(\beta G)_{T_1,s} - (\beta G)_{T_i,s}\}$ is known,[57] where the expression $(\beta G)_{Tm,n}$ indicates (βG) for the meta-stable phase n at

the state point T_{am}. Given that T_{am}, an approximate melting point, is the state point at which the thermodynamic integration is conducted, the following can be obtained:

$$[(\beta G)_{T_1,s} - (\beta G)_{T_{am},s}] + [\beta(G_{T_{am},s} - G_{T_{am},l})]$$
$$-[(\beta G)_{T_i,l} - (\beta G)_{T_{am},l}] = [(\beta G)_{T_1,s} - (\beta G)_{T_i,l}]. \quad (9)$$

Equation (9) further can be rewritten as

$$[(\beta G)_{T_1,s} - (\beta G)_{T_{am},s}] + [\beta(G_{T_{am},s} - G_{T_{am},l})]$$
$$+[(\beta G)_{T_1,l} - (\beta G)_{T_i,l}] - [(\beta G)_{T_1,l} - (\beta G)_{T_{am},l}]$$
$$= [(\beta G)_{T_1,s} - (\beta G)_{T_i,l}], \quad (10)$$

where the first, third, and fourth terms on the left side of Eq. (10) are obtained from the MHR analysis; while the second term comes from the pseudo-supercritical path by free energy calculation.

5. Melting temperature from kinetic approach

The Lindemann parameter and non-Gaussian parameter are used in this work to estimate the kinetic melting temperature. The Lindemann criterion[65] is widely used to determine the melting temperature of a solid. It states that melting is a vibrational lattice instability initiated when the root-mean-square (RMS) displacement of atoms reaches a critical fraction of the inter-atomic distance:

$$\sqrt{\langle \Delta r^2 \rangle} = \delta_L a, \quad (11)$$

where δ_L is the Lindemann parameter, a is the nearest neighbor distance, and $\Delta r = |r_i(t) - R_i|$; r_i is the instantaneous position of atom i and R_i is the equilibrium position of atom i.

Large deviations of solid particles near the melting temperature can be expressed using the non-Gaussian parameter:

$$\alpha_2(t) = \frac{\langle \Delta r^4 \rangle}{(1 + 2/d)\langle \Delta r^2 \rangle^2} - 1. \quad (12)$$

Here, d is the spatial dimension and $\langle \cdots \rangle$ denotes ensemble averaging.

The value of $\alpha_2(t)$ is very small, and is weakly dependent on temperature at lower temperatures. At a certain temperature, $\alpha_2(t)$ suddenly jumps as a result of the strong deviation of atoms from their equilibrium lattice position. This is an indication of the melting temperature. Subsequently, $\alpha_2(t)$ drops to zero, when crystal loses its crystallinity completely, in a random liquid.[37,66,67] The non-Gaussian parameter can be used to detect the melting point of a solid, as shown by Jin et al.[37] Moreover, it along with the Lindemann parameter can also be used to detect the melting point of simple solids in slit pores, albeit not for very attractive pore.[18]

III. SIMULATION DETAILS

The thermodynamic melting temperature is evaluated where the Gibb's free energy difference between the solid and liquid phases is equal to zero. First, we select an approximate melting temperature, T_{am}, by performing two different types of $NP_{zz}AT$ simulation using LAMMPS.[68] The velocity-Verlet

algorithm is used to integrate the equation of motion with a time step, $\Delta t = 4$ fs. The temperature and pressure are controlled using a Nosé–Hoover thermostat and barostat[69] with relaxation times of 2 ps and 5 ps for temperature and pressure, respectively. Approximately 4000–60 000 particles are used, depending on the pore size. Truncated and shifted potential is used with a cutoff radius of 5σ for both the particle-particle and wall-fluid interactions. The periodic boundary condition is employed in the axial direction (z direction) of the cylindrical pore. The pressure component along the periodic dimension, P_{zz}, is kept fixed to unity. To construct the Gibbs free energy curves of the crystalline and liquid phases under confinement, using MHR, histograms are collected from $NP_{zz}AT$ molecular dynamics simulations. We perform 11 simulations for each phase. The temperature for each simulation is chosen according to the following relationship:

$$T_i = T_{am} + \sum_{n=-5}^{5} n\Delta T,$$

where T_{am} is the approximate melting temperature estimated from the hysteresis data; ΔT is chosen in accordance with the meta-stable region.

The initial configurations for solid-phase or liquid phase simulations are taken from the NPT simulation run used for hysteresis analysis. After sufficient equilibration, for around 200 ps, simulations are conducted for an additional 10 ns. The reference state points are selected at the lowest temperature, $T_i = T_{am} - 5\Delta T$. The system's potential energy U and volume V are recorded at every time step, and these data are converted into histograms.

The thermodynamic integration calculations, during the three-stage pseudo-supercritical path, are conducted using NVT molecular dynamics. The temperature is maintained using Nosé-Hoover thermostat algorithm. The Gaussian potential well parameters are chosen as per Grochola.[64] The value of the scaling parameter is kept fixed at $\eta = 0.1$.[57]

Simulations for the first stage of the transformation path are started from a random initial configuration (i.e., $\lambda = 0$), which is obtained during thermal cycle runs. Subsequently for each λ initial configuration is taken from its previous λ simulation. For all the three stages time step is fixed at 4 fs, and total simulation run for each λ is 20 ns. For the second stage, stage b, we take the last configuration of the stage-a as the initial configuration. However, to obtain the final configuration we put dummy atoms on the crystal lattice obtained from the heating cycle run. In order to assess the error for this stage we have considered 3–4 initial crystal configurations (obtained from the hysteresis runs). The Gaussian potential wells are attached to these dummy atoms. The initial configuration for the third stage is taken from the heating run of hysteresis loop at T_{am} and the dummy atoms are created as described for the second stage. Thermodynamic integration is conducted using the standard ten point Gauss-Legendre integration scheme for all the stages. Block average is used to obtain the error in the data points.

IV. RESULTS AND DISCUSSION

In our previous note[19] we discussed the thermodynamics melting temperature in slit pores. It was found that melting temperatures at larger slit pore with width >10 obey the Gibbs-Thomson equation. However, melting temperature is oscillatory in nature for narrower pores of size less than 10. This phenomenon in slit pores has attracted our attention towards cylindrical pores. We first discuss the possibilities of evaluating the melting temperature using the kinetic approach. Figure 3 presents the non-Gaussian and Lindemann parameters with temperature. In case of pore size with pore radius, $R = 6$, non-Gaussian parameter exhibits multiple maximum over a wide temperature range, making it impossible to use the data to obtain any reasonable estimate of the melting temperature. Hence, it is difficult to determine the melting temperature in cylindrical confinement for lower pore size from the kinetic approach unlike the case of slit pores.[18] However, for higher pore size, non-Gaussian parameter can be implemented as shown for $R = 12$ in Fig. 3(bottom panel). On the other hand, the application of Lindemann parameter to estimate the melting temperature completely depends on its crystal structure, and does not agree with the value estimated from the non-Gaussian parameter. Hence the kinetic approach suffers from various problems to locate the melting temperature in cylindrical confinement.

Now, we turn our attention to the thermodynamics approach to evaluate the melting temperature in cylindrical pores. As earlier mentioned, the first step of evaluating the true thermodynamic melting temperature is to determine an approximate melting temperature, which is done using hysteresis loop along the phase transition. We first calculate the overall density of the confined system along the quenching
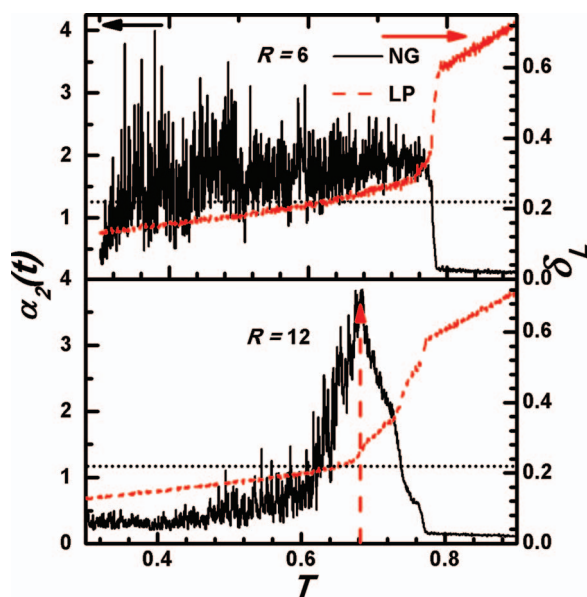

FIG. 4. Density as a function of temperature for solid and liquid phases at $P_{zz} = 1.0$ for pore radius, $R = 12$, for $\varepsilon_{wf} = 0.4348$, $\alpha = 2.32$. Symbols square and circle represent quenching and heating cycles, respectively. The solid (top curve) progressively heated from $T = 0.3$ to 0.81, while the liquid (bottom) is quenched progressively from $T = 1.2$ to 0.3. Vertical dotted line indicates an approximate melting temperature (T_{am}). Horizontal dotted lines indicate corresponding densities of solid and liquid at T_{am}.

and heating paths. Figure 4 presents a plot of density as a function of temperature for the heating and cooling cycles, for a pore radius $R = 12$. As the liquid is quenched, the density gradually increases with lowering in temperature, and from $T = 0.75$ until $T = 0.6$ rate of increase in the density is relatively high before turning again to the monotonic behavior of increasing density with lowering in temperature. We observe a clear hysteresis loop, which for $R < 4$ is found to disappear, as also experimentally observed in a recent study of water in silica pore.[34] The hysteresis loop indicates a first order phase transition. A wide meta-stable region is observed around the true crossover point. The melting point is adjacent to this meta-stable region. It clearly shows that abrupt density change or a discontinuous drop in density occurs at $T \sim 0.78$, which indicates that the true thermodynamic melting temperature would be lower than this temperature. In Fig. 4 vertical dashed line represents the approximate melting temperature $T_{am} = 0.69$, at which free energy difference is evaluated using pseudo-supercritical transformation path. Solid and liquid box lengths are determined from the corresponding densities as shown by horizontal dotted lines in Fig. 4.

Figure 5 presents the density profile along the radial direction for pore radius, $R = 12$. Figure 5 (panel (a)) illustrates the local density profile at various temperatures. The local density is significantly large near the wall, even at $T = 0.78$, indicative of solid like behavior of the contact layer. With the distance away from the wall, the wall effect is diminished, and the density is found to reduce. In general, at higher temperatures, heights of the peaks of the layers are not pronounced particularly near the centre of the pore. As temperature decreases, the heights of the peaks increase, and for lower temperature, where the solid phase clearly appears, sharp distinct peaks are observed. Figure 5 (panel (b)) shows the density profiles for solid and liquid phases at the approximate melting temperature along the radial direction. Wall effect is clearly evident even in the liquid phase particularly near the wall, indicated by the sharp peaks in the density profiles. However, that is seen to diminish near the centre of the pore.

FIG. 3. The Lindemann parameter, δ_L, and non-Gaussian parameter, $\alpha_2(t)$, as a function of temperature. Vertical dashed arrow line from the bottom indicates the melting temperature, where $\alpha_2(t)$ is maximum. Firm horizontal arrow lines represent the corresponding axes. Horizontal dotted line indicates the critical Lindemann parameter. Presence of multiple high peaks makes it hard to evaluate the melting point for lower pore radius.
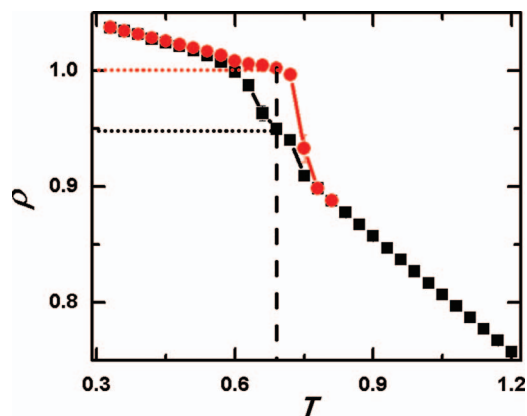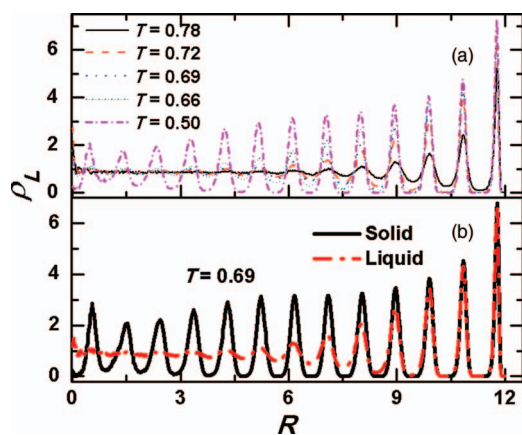
FIG. 5. (a) Local density (ρ_L) as a function of radial distance from the centre of the pore for $R = 12.0$, quenching case. The orientation of the particles near the wall surface is ordered but disordered at the proximity of the centre of the pore. (b) The comparison of local density profile for solid and liquid at an approximate melting temperature (0.69). In case of liquid, particles are ordered near the wall surface, but are disordered after few layers away from the wall—indicative of the liquid phase. On the other hand, solid density peaks are more pronounced throughout the pore indicative of the crystalline phase at T_{am}.
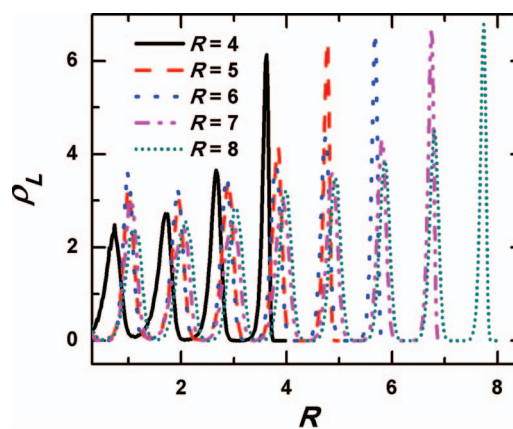

FIG. 6. Local density (ρ_L) as a function of radial distance from the centre of the pore at $T = 0.69$, for the heating case.

This is clearly not the case for the solid phase, which shows clear sharp peak even at the centre of the pore. We estimate in-plane order parameter: $\psi_k = \langle \frac{1}{N_b} | \sum_{j=1}^{N_b} \exp(ik\theta_j) | \rangle$, where k = 4 and 6 represent square and triangular symmetry, respectively; N_b is the total number of near neighbors at a distance of 1.5 in each layer, and θ_j is the angle formed by a particle with its nearest-neighbor atom. Table I summarizes the bond orientation order parameters value. Contact layers indicate a very high value of ψ_6 compared to ψ_4, indicative of dominance of triangular symmetry in the solid phase. Even in the liquid phase first three layers from the wall are of high order, and particles in these layers are in triangular symmetry. Figure 6 presents the local density along radial direction for different pore radius at $T = 0.69$. For lower pore, $R < 10$, the heights of the central peaks are more compared to that of the higher pores. Hence, in cylindrical pore surface effect is quite

dominant and freezing in cylindrical pore is an intricate succession of transitions where different layers freeze at a wide range of conditions. Similar kind of behavior is also observed in earlier studies.[20,45]

In order to estimate the thermodynamic melting temperature, Gibbs free energy curves are constructed taking $T = 0.69$ as an intermediate point of the meta-stable region. Simulations are performed at 11 different temperatures, as described earlier. For each temperature, two sets of simulations are performed, viz. one for the heating case and another for the quenching case, resulting in 22 histograms. Figure 7 presents the Gibbs free energy curves for the solid and liquid phases with respect to their respective reference states. The next step is the determination of Gibbs free energy difference between the two phases at an approximate melting temperature.

Thermodynamic integration is conducted at an approximate melting temperature along the pseudo-supercritical path, through which solid and liquid phases are connected avoiding the first order phase transition. The box lengths for solid and liquid phases are determined from their respective densities as shown in Fig. 4. The box lengths are chosen such a way that $P_{zz} = 1$ remains constant at the beginning of the stage-a and at the end of the stage-c which is shown in Fig. 8. We also observed overall pressure to remain constant. Plots of

TABLE I. Bond order parameters for each layer at an approximate melting temperature for solid and liquid phases, for pore radius $R = 12$.

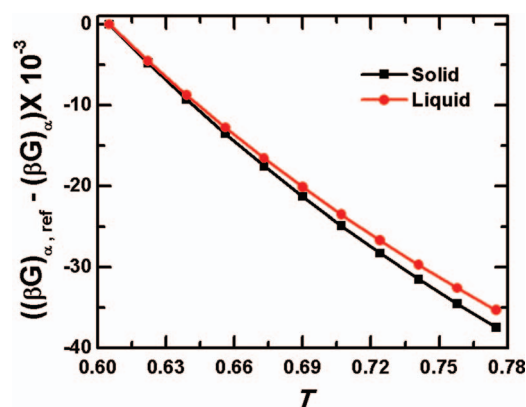| R	Layer	Ψ_4		Ψ_6	
		Solid	Liquid	Solid	Liquid
12	Contact layer	0.062	0.0978	0.744	0.719
	2nd layer	0.099	0.034	0.780	0.739
	3rd layer	0.075	0.061	0.786	0.700
	4th layer	0.032	0.063	0.762	0.520
	5th layer	0.073	0.052	0.728	0.245
	6th layer	0.233	0.043	0.708	0.080
	7th layer	0.218	0.052	0.718	0.067
	8th layer	0.263	0.054	0.706	0.065
	9th layer	0.374	0.056	0.579	0.068
	10th layer	0.239	0.075	0.469	0.077
	11th layer	0.171	0.090	0.239	0.094
	Centre layer	0.289	0.164	0.242	0.159

FIG. 7. Relative Gibbs free energy curves as a function of temperature for confined Lennard-Jones system for $R = 12$ relative to the respective reference states for the liquid and solid phases, constructed from MHR.
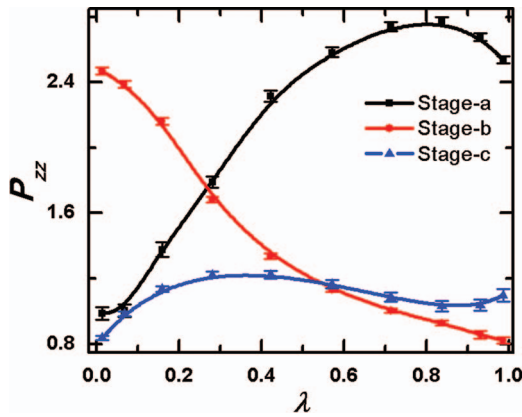
FIG. 8. P_{zz} as a function of λ during the three stages, for $R = 12$. Pressure at the beginning of stage-a and pressure at the end of stage-c remain same, which is the essential characteristic for the three-stage pseudo-supercritical transformation path.

FIG. 9. $\langle \partial U / \partial \lambda \rangle_{NVT\lambda}$ as a function of λ for three-stage pseudo-supercritical transformation path for the confined Lennard-Jones system, for $R = 12$, at an approximate melting temperature.

$\langle \partial U / \partial \lambda \rangle_{NVT\lambda}$ as function of λ for three stages of thermodynamic integration are shown in Fig. 9, which shows that the curves are continuous and integrable for all the three stages. Moreover, we have also checked the reversibility of the thermodynamic path considered in this work. For all the three cases error bars are of the order of symbol size. The different contributions to the Gibbs free energy for all the pore sizes are presented in Table II.

Once the Gibbs free energy difference of two phases, ΔG, is determined at an approximate melting temperature, it is no longer difficult to convert liquid Gibbs free energy curve relative to a solid reference state using Eq. (10). The two Gibbs free energy curves with respect to the solid reference state point are shown in Fig. 10. Using the relative free energy between the crystalline and liquid phases at a single point, the free energy difference between crystalline and liquid phases can be evaluated for all other points. By determining ΔG in this way over a range of temperatures, ΔG can be presented as a function of temperature, and the temperature where ΔG is zero indicates a single coexistence point or thermodynamic melting temperature, as shown in Fig. 11. The coexistence temperature calculated using the above mentioned method for $R = 12$ is 0.745. Table II summarizes
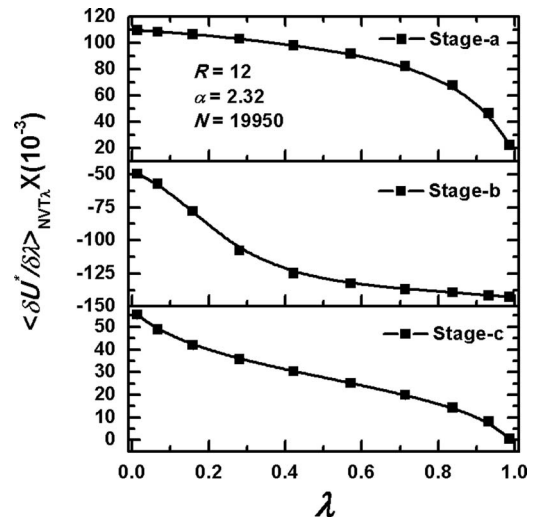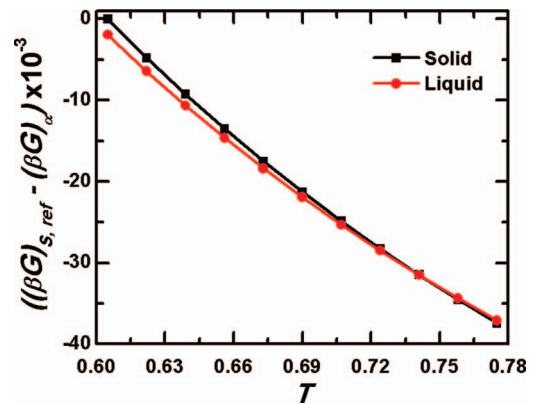

FIG. 10. Relative Gibbs free energy as a function temperature for $R = 12$ constructed from MHR. Both branches are relative to the solid reference state.

TABLE II. Estimated true thermodynamic melting temperature, T_m, and different contributions to the Gibbs free energy, for different pore radii, R, at an approximate melting temperature (T_{am}) are presented. ΔG denotes Gibbs free energy difference at T_{am}. ρ_L and ρ_S represent corresponding densities of liquid and solid, respectively, at T_{am}. By using block averaging, errors are estimated for individual data points. These errors are then integrated to estimate the final error.

| R	T_{am}	ρ_L	ρ_S	ΔA^{ex}	ΔA^{id}	$P\Delta V$	ΔG	T_m
				Wall (LJ 9-3) $\varepsilon_{wf} = 0.4348$, $\alpha = 2.32$				
20	0.70	0.946	0.985	-1613.47 ± 0.28	-1545.73	2287.82	-2355.55	0.765 ± 0.001
16	0.69	0.951	0.985	-560.34 ± 0.34	865.71	-1296.53	-991.17	0.758 ± 0.001
12	0.69	0.950	1.002	-88.55 ± 0.40	742.36	-1102.84	-449.03	0.745 ± 0.001
10	0.69	0.944	0.972	29.61 ± 0.47	285.72	-432.30	-116.96	0.735 ± 0.002
8	0.69	0.960	1.005	-3.03 ± 0.55	277.45	-409.39	-134.98	0.722 ± 0.002
7	0.72	0.931	1.003	-1.63 ± 0.64	362.27	-520.82	-160.19	0.762 ± 0.002
6	0.72	0.916	0.984	-1.57 ± 0.75	258.60	-378.43	-121.41	0.754 ± 0.002
5	0.75	0.938	0.971	-1.46 ± 0.98	88.66	-123.87	-36.67	0.769 ± 0.002
4	0.72	0.894	0.945	-4.92 ± 1.11	82.95	-125.41	-4739	0.747 ± 0.004
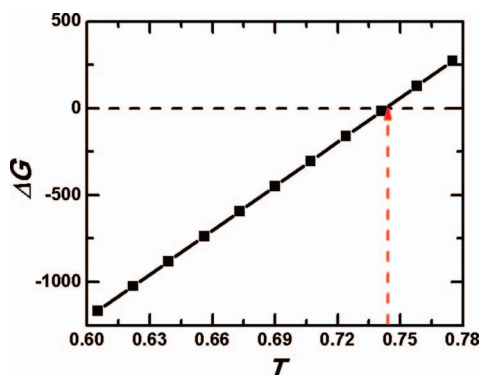
FIG. 11. ΔG as a function of T for $R = 12$. Vertical arrow dashed line indicates solid-liquid coexistence temperature or true thermodynamic melting temperature (T_{m}) of solid.

different contributions to the Gibbs free energy and the estimated true thermodynamic melting temperatures for different pore sizes.

In this work, we have observed depression of the melting temperature under cylindrical confinement. However, no specific relation is found for the melting temperature with the pore size. Instead, oscillatory nature of the melting temperature, for narrow pores, is seen similar to the behavior observed by earlier worker using different methods.[22, 48, 49] Interestingly, depression of the melting temperature, with respect to the bulk value, is observed for almost all pore radii (see Table II). In our earlier work in slit pore, for strong wall-fluid interaction ($\alpha = 2.32$),[18] we have reported elevation and depression in the kinetic temperature depending on the pore size. However, for the case of thermodynamic melting temperature, elevation is observed. Interestingly, in this work we observe only depression in the thermodynamic melting temperature compared to that of the bulk solid. It is now clear that the oscillatory behavior in the melting temperature (kinetic or thermodynamic) in narrow pores is a generic behavior, as also supported by our earlier works.[18, 19] However, at higher pore sizes the melting temperature is close to its bulk value, which indicates that the effect of confinement gradually diminishes with increasing pore radius. The melting temperature at higher $R > 8$ is in linear relationship with inverse of the pore size, and obeys the Gibbs-Thomson equation. Fig. 12 presents plot of the scaled shift in T_m [$(T_{mc} - T_{mb})/T_{mb}$] against the inverse of pore radius, where T_{mb} is the
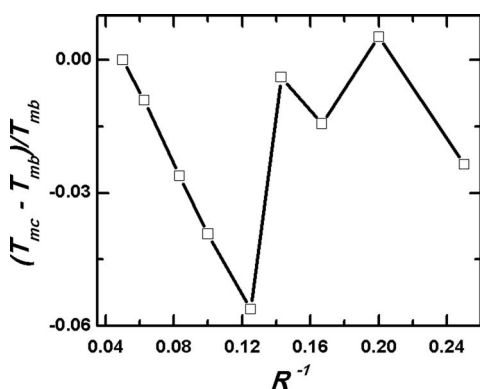
bulk melting temperature, and T_{mc} is the melting temperature under confinement. At lower pore sizes, this equation often fails as the reduced density of the confined fluids differs from the bulk value.[6, 31–33] We have taken bulk melting temperature as 0.765 in accordance with Eike et al.[57] Based on the results in this work, wall effect disappears beyond $R = 20$, as the thermodynamic melting temperature reaches the bulk value. This phenomenon is also supported by earlier work,[45] which reported that for pore diameters greater than 20 molecular diameters the confined fluids freeze into a single crystalline structure.

V. CONCLUSION

In this work, we have demonstrated the melting behavior of LJ solids confined in strongly attractive cylindrical pores of different pore radii. Thermodynamic melting temperatures of confined LJ fluids are evaluated using a pseudo-supercritical transformation path connecting the solid and liquid phases without the first order phase transition along with the multiple histogram reweighting technique. Thermal cycling produces pronounced hysteresis associated with the first order phase transition. However, hysteresis is found to disappear for $R < 4$. The thermodynamic melting temperature for almost all pore radii is lower than the bulk case, which is contrary to the behavior seen in slit pores. The melting temperatures at lower pore sizes are oscillatory in nature. For $R > 8$ the thermodynamic melting temperatures are in linear relationship with inverse of the pore radius as predicted by the Gibbs-Thomson equation.

[1]J. B. Murton, R. Peterson, and J.-C. Ozouf, Science **314**(5802), 1127 (2006).
[2]M. Muthukumar, Annu. Rev. Biophys. Biomol. Struct. **36**, 435 (2007).
[3]M. Alcoutlabi and G. B. McKenna, J. Phys.: Condens. Matter **17**, R461 (2005).
[4]P. T. Cummings, H. Docherty, C. R. Iacovella, and J. K. Singh, AICHE J. **56**(4), 842 (2010).
[5]L. D. Gelb, K. E. Gubbins, R. Radhakrishnan, and M. Sliwinska-Bartkowiak, Rep. Prog. Phys. **62**, 1573 (1999).
[6]C. Alba-Simionesco, B. Coasne, G. Dosseh, G. Dudziak, K. E. Gubbins, R. Radhakrishnan, and M. Sliwinska-Bartkowiak, J. Phys.: Condens. Matter **18**, R15 (2006).
[7]M. Miyahara and K. E. Gubbins, J. Chem. Phys. **106**, 2865 (1997).
[8]A. Z. Panagiotopolos, Mol. Phys. **62**(3), 701 (1987).
[9]B. K. Peterson, K. E. Gubbins, G. S. Heffelfinger, U. Marini, B. Marconi, and F. van Swo, J. Chem. Phys. **88**(10), 6487 (1988).
[10]R. Evans, U. Marini, B. Marconi, and P. Tarazona, J. Chem. Phys. **84**, 2376 (1986).
[11]S. K. Singh, J. K. Singh, S. K. Kwak, and G. Deo, Chem. Phys. Lett. **494**, 182 (2010).
[12]S. K. Singh and J. K. Singh, Fluid Phase Equilib. **300**, 182 (2011).
[13]S. K. Singh, S. Khan, S. Jana, and J. K. Singh, Mol. Simul. **37**, 350 (2011).
[14]S. K. Singh, A. Sinha, G. Deo, and J. K. Singh, J. Phys. Chem. C **113**, 7170 (2009).
[15]S. Jana, J. K. Singh, and S. K. Kwak, J. Chem. Phys. **130**, 214707 (2009).
[16]P. C. Ball and R. Evans, Mol. Phys. **63**(1), 159 (1988).
[17]L. Firlej and B. Kuchta, Mater. Sci.-Poland **24**(2), 443 (2006).
[18]C. K. Das and J. K. Singh, Theor. Chem. Acc. **132**, 1351 (2013).

FIG. 12. Shift in the melting temperature reduced by the bulk melting temperature as a function of inverse of the pore radius, R.

[19]C. K. Das and J. K. Singh, J. Chem. Phys. **139**(17), 174706 (2013).

[20]M. W. Maddox and K. E. Gubbins, J. Chem. Phys. **107**(22), 9659 (1997).

[21]T. Kaneko, K. Yasuoka, and X. C. Zeng, Mol. Simul. **38**(5), 373 (2012).

[22]T. Kaneko, T. Mima, and K. Yasuoka, Chem. Phys. Lett. **490**, 165 (2010).

[23]J. A. Duffy, N. J. Wilkinson, H. M. Fretwell, and M. A. Alam, J. Phys.: Condens. Matter **7**, L27 (1995).

[24]K. M. Unruh, T. E. Huber, and C. A. Huber, Phys. Rev. B **48**(12), 9021 (1993).

[25]J. Klein and E. Kumacheva, Science **269**, 816 (1995).

[26]C. A. Murray and D. H. V. Winkle, Phys. Rev. Lett. **58**(12), 1200 (1987).

[27]Y. Tang, A. J. Armstrong, R. C. Mockler, and W. J. O. Sullivan, Phys. Rev. Lett. **62**(20), 2401 (1989).

[28]J. Warnock, D. D. Awschalom, and M. W. Shafer, Phys. Rev. Lett. **57**(14), 1753 (1986).

[29]J. Klein, D. Perahia, and S. Warburg, Nature **352**, 143 (1991).

[30]R. W. Bathelor and A. G. Foste, Trans. Faraday Soc. **40**, 300 (1944).

[31]D. Morineau, Y. Xia, and C. Alba-Simionesco, J. Chem. Phys. **117**, 8966 (2002).

[32]D. Morineau, R. Guegan, Y. Xia, and C. Alba-Simionesco, J. Chem. Phys. **121**(3), 1466 (2004).

[33]C. Alba-Simionesco, G. Dosseh, E. Dumont, B. Frick, B. Geil, D. Morineau, V. Teboul, and Y. Xia, Eur. Phys. J. E **12**, 19 (2003).

[34]S. Jähnert, F. V. Chávez, G. E. Schaumann, A. Schreiber, M. Schönhoff, and G. H. Findenegg, Phys. Chem. Chem. Phys. **10**, 6039 (2008).

[35]H. Dominguez, M. P. Allen, and R. Evans, Mol. Phys. **96**(2), 209 (1999).

[36]M. Schmidt and H. Löwen, Phys. Rev. Lett. **76**(24), 4552 (1996).

[37]Z. H. Jin, P. Gumbsch, K. Lu, and E. Ma, Phys. Rev. Lett. **87**(5), 055703 (2001).

[38]A. V. Granato, D. M. Joncich, and V. A. Khonik, Appl. Phys. Lett. **97**, 171911 (2010).

[39]M. Born, J. Chem. Phys. **7**, 591 (1939).

[40]F. Delogu, J. Phys.: Condens. Matter **18**(24), 5639 (2006).

[41]J. P. Hansen and L. Verlet, Phys. Rev. **184**(1), 151 (1969).

[42]W. Gotze and M. Liicke, J. Low Temp. Phys. **25**(5/6), 671 (1976).

[43]J. Q. Broughton, G. H. Gilmer, and J. D. Weeks, Phys. Rev. B **25**(7), 4651 (1982).

[44]S. Ranganathan and K. N. Pathak, Phys. Rev. A **45**(8), 5789 (1992).

[45]M. Sliwinska-Bartkowiak, G. Dudziak, R. Sikorski, R. Gras, R. Radhakrishnan, and K. E. Gubbins, J. Chem. Phys. **114**(2), 950 (2001).

[46]R. Radhakrishnan, K. E. Gubbins, and M. Sliwinska-Bartkowiak, J. Chem. Phys. **116**(3), 1147 (2002).

[47]R. Radhakrishnan and K. E. Gubbins, J. Chem. Phys. **111**(19), 9058 (1999).

[48]R. Radhakrishnan, K. E. Gubbins, and M. Sliwinska-Bartkowiak, J. Chem. Phys. **112**(24), 11048 (2000).

[49]L. Wan, C. R. Iacovella, T. D. Nguyen, H. Docherty, and P. T. Cummings, Phys. Rev. B **86**, 214105 (2012).

[50]M. Sliwinska-Bartkowak, F. R. Hung, E. E. Santiso, B. Coasne, G. Dudziak, F. R. Siperstein, and K. E. Gubbins, Adsorption **11**, 391 (2005).

[51]H. C. Huang, S. K. Kwak, and J. K. Singh, J. Chem. Phys. **130**, 164511 (2009).

[52]C. H. Huang, W. W. Chen, J. K. Singh, and S. K. Kwak, J. Chem. Phys. **132**, 224504 (2010).

[53]F. J. Durán-Olivencia and M. C. Gordillo, Phys. Rev. E **79**, 061111 (2009).

[54]E. D. Glandt, J. Colloid Interface Sci. **77**(2), 512 (1980).

[55]I. Brovchenko, A. Geiger, and A. Oleinikova, J. Chem. Phys. **120**(4), 1958 (2004).

[56]D. W. Siderius and L. D. Gelb, J. Chem. Phys. **135**, 084703 (2011).

[57]D. M. Eike, J. F. Brennecke, and E. J. Maginn, J. Chem. Phys. **122**, 014115 (2005).

[58]A. M. Ferrenberg and R. H. Swendsen, Phys. Rev. Lett. **61**, 2635 (1988).

[59]A. M. Ferrenberg and R. H. Swendsen, Phys. Rev. Lett. **63**, 1195 (1989).

[60]J. Chang and S. I. Sandler, J. Chem. Phys. **118**(18), 8390 (2003).

[61]J. Chang, A. M. Lenhoff, and S. I. Sandler, J. Chem. Phys. **120**(6), 3003 (2004).

[62]K. Kiyohara, K. E. Gubbins, and A. Z. Panagiotopoulos, J. Phys. Chem. **106**(8), 3338 (1997).

[63]P. B. Conrad and J. J. d. Pablo, Fluid Phase Equilib. **150–151**, 51 (1998).

[64]G. Grochola, J. Chem. Phys. **120**(5), 2122 (2004).

[65]F. A. Lindemann, Z. Phys. **11**, 609 (1910).

[66]A. Rahman, Phys. Rev. **136**(2A), A405 (1964).

[67]B. Vorselaars, A. V. Lyulin, K. Karatasos, and M. A. J. Michels, Phys. Rev. E **75**, 011504 (2007).

[68]S. J. Plimpton, J. Comput. Phys. **117**, 1 (1995).

[69]G. J. Martyna, M. E. Tuckerman, D. J. Tobias, and M. L. Klein, Mol. Phys. **87**, 1117 (1996).